Title

The Underlying Chemical Mechanism of Selective Chemical Etching in CsPbBr3 Nanocrystals for Reliably Accessing Near-Unity Emitters

Journal

ACS Nano, 13(10)

ISSN

1936-0851

Authors

Koscher, Brent A
Nett, Zachary
Alivisatos, A Paul

Publication Date

2019-10-22

DOI

10.1021/acsnano.9b05782

Peer reviewed

The underlying chemical mechanism of selective chemical etching in $CsPbBr_3$ nanocrystals for reliably accessing near-unity emitters

Brent A. Koscher[1,3,4], Zach Nett[1,3,4], and A. Paul Alivisatos[1,2,3,4*]

[1] Department of Chemistry, University of California, Berkeley, CA 94720, USA.

[2] Department of Materials Science and Engineering, University of California, Berkeley, CA 94720, USA.

[3] Materials Science Division, Lawrence Berkeley National Laboratory, Berkeley, CA 94720, USA.

[4] Kavli Energy NanoScience Institute, Berkeley, CA 94720, USA.

ABSTRACT: Reliably accessing nanocrystal luminophores with near-unity efficiencies aids in the ability to understand the upper performance limits in optoelectronic applications that require minimal non-radiative losses. Constructing structure-function relationships at the atomic level, while accounting for inevitable defects, allows for the development of robust strategies to achieve near-unity quantum yield luminophores. For $CsPbBr_3$ perovskite nanocrystals, bromine vacancies leave behind under-coordinated lead atoms that act as traps, limiting the achievable optical performance of the material. We show that selective etching represents a promising path for mitigating the consequences of optical defects in $CsPbBr_3$ nanocrystals. A mechanistic understanding of the etching reaction is essential for developing strategies to finely control the reaction. We report a study of the selective etching mechanism of $CsPbBr_3$ nanocrystal cubes by controlling the etchant chemical potential. We observe optical absorption and luminescence trajectories while varying the extent and rate of lead removal, removing in some cases up to 75% of the lead from the original nanocrystal ensemble. At modest etchant chemical potentials, the size and shape uniformity of the nanocrystal ensemble improves in addition to the quantum yield, proceeding through a layer-by-layer etching mechanism. Operating with excessively high etchant chemical potentials is detrimental to the overall optical performance as the etching transitions to non-selective, while too low of a chemical potential results in incomplete etching. Through this general approach, we show how to finely control selective etching to consistently access a steady state or chemical stability zone of near-unity quantum yield $CsPbBr_3$ nanocrystals post-synthetically, suggesting a practical framework to extend this treatment to other lead halide compositions and sizes.

Introduction

Luminophore optical and material quality dictates the performance limits in several optoelectronic applications – light-emitting diodes[1-3], photodetectors[4,5], and photovoltaics[6-9], among others. In order to probe the upper bounds of performance in these applications, robust strategies to reliably access high photoluminescence quantum yield (PLQY) are being developed[10-15]. While there has been success in approaching near-unity PLQY luminophores in traditional quantum dot systems, all-inorganic cesium lead halide perovskite ($CsPbX_3$; X = Cl, Br, I) nanocrystals are relatively new candidates for high-efficiency luminophores[16,17]. The $CsPbX_3$ nanocrystals have received substantial interest due to their exceptional optoelectronic properties, including strong optical absorptions, narrow linewidths, and high PLQYs, all without requiring the overgrowth of an epitaxial passivating semiconductor shell[16-19]. Several investigations already report notable performances of $CsPbX_3$ nanocrystals in light-emitting diodes[3,20-22], low-threshold lasers[23], and photovoltaics[9]. Additionally, due to the combination of high PLQYs and fast radiative rates, these nanocrystals are promising candidates for controllable and wavelength-tunable single-photon sources[24,25], and new photonic applications[26,27]. For each of these applications, the optical quality of the material employed is directly related to its overall performance. While the high optical quality of the lead halide perovskites is often attributed to an unusual level of inherent defect tolerance[28-30], they are not defect impervious. Calculations and experiments suggest non-negligible defects that can be present in the material[12,14,15,28-31], the concentration of which depends on precursor stoichiometries employed during the synthesis[28,31]. Developing strategies to mitigate the presence of defect states in $CsPbX_3$ nanocrystals represents a promising path towards creating the highest optical quality materials that probe the upper limits of efficiency. While we focus on $CsPbBr_3$ nanocrystals herein, lessons learned can inform rational paths forward to improve the optical performance of other compositions.

The weak internal chemical bonding of lead halide perovskites is an important factor that enables facile synthesis under mild conditions and contributes to the large ionic mobilities within the lattice[19,32-34]. This weak internal bonding also contributes to long-term stability issues and increased susceptibility to the creation of defects[28-31,34]. The chance is further increased due to the lead-rich synthesis conditions and the lability of surface-bound oleylammonium bromide ligands[12,35,36]. Given these conditions, the presence of bromine vacancies represents one of the more prevalent defects present in as-synthesized $CsPbBr_3$ nanocrystals. A bromine vacancy results in an under-coordinated lead atom, which has been shown to introduce a shallow electron state below the conduction band[12,15,28,31]. These cumulative defects contribute to non-radiative recombination attributed to sub-unity PLQYs and extended multi-exponential excited state decay channels typical in $CsPbBr_3$ samples[12-16,20]. Recently defects in $CsPbX_3$ nanocrystals are starting to be systematically explored and the understanding of the optoelectronic consequences of these defects is continuing to expand. Comprehensive chemical strategies to post-synthetically target bromine vacancies are critical to access the highest quality $CsPbBr_3$ nanocrystals for both optical and electronic applications.

Proposed methods to mitigate the effects of undercoordinated lead atoms fall in three categories: ligand passivation of defect states[12,20,22,35,36], shifting the dynamic surface equilibrium towards increased surface-bound halide[13,21,37], and selective etching of surface under-coordinated lead[14,15]. The first two strategies can work well for select circumstances, improving the PLQYs up to ~95%[12,13]. However, these strategies require introducing a significant excess of ligands or bromide sources to shift the equilibrium towards passivation. They also ultimately encounter steric and entropic limitations, making it difficult to fully passivate all the defects present in a controlled fashion[12,13,35-37]. However, selective chemical etching[14,15] offers an appealing alternative that is not constrained like the approaches described above. Further, precise control of the reactive etchant chemical potential can be used to achieve higher levels of selectivity[38-40]. Selective etching has been successfully employed for epitaxial liftoff processes[40,41] and to control the surface properties of thin film semiconductors. This approach also allows for the optimization of the primary etching pathway while mitigating the presence of unfavorable side reactions. Atoms within specific local bonding environments are post-synthetically targeted by modulating the etchant chemical potential, a potentially powerful tool that can be used to improve the PLQY of nanocrystal ensembles. Traditional quantum dot semiconductors have stronger internal bonding compared to the ionic lead halide perovskites, typically resulting in either modest PLQY improvements or degradation of the optical performance through chemical etching[42-44]. Careful tuning of the etching conditions is necessary in order to achieve good results. Here we find an opportunity to harness the inherent weak chemical bonding of $CsPbBr_3$ to allow for tuning of the etchant chemical potential under mild conditions to achieve selective etching of under-coordinated lead atoms. To this end, we previously demonstrated a post-synthetic thiocyanate treatment capable of improving the PLQY of as-synthesized and aged $CsPbBr_3$ nanocrystals from 60% to near-unity by reducing nanocrystal lead richness[12,14,15]. Here we build on this work to provide a more complete description of the underlying mechanism of selective etching in $CsPbBr_3$ nanocrystals and to provide a more general framework for approaching the chemical modification of the all inorganic colloidal perovskite lead halide nanocrystals.

Results and Discussion

To understand the underlying mechanism of the thiocyanate etching reaction, first we consider the etching conditions from our previous report[15]. We use $CsPbBr_3$ nanocrystal cubes that are isolated from the reaction mixture by centrifugation[16] (synthetic details in Supporting Information) and then maintained as a colloidal solution in a non-polar solvent. During the synthesis, both oleic acid and oleylamine ligands are employed to solubilize the precursors for the nanoparticle synthesis and to afterwards maintain nanocrystal colloidal stability. Although there is a geometrically ideal packing density of ligands on the surface[35] (~2.9 nm^2), after synthesis there are more ligands present in solution (6 nm^2) than required to fully passivate the surface (Supporting Information). Due to the dynamic nature of ligand binding in these materials, excess ligands have been shown to play an important role in shifting the equilibrium towards surface bound species[12,35,36]. To the as-isolated $CsPbBr_3$ sample, a dry powder of either ammonium or sodium thiocyanate is added and stirred at room temperature. Following completion of the treatment, the absorption spectrum is largely unchanged but there is a significant change in the photoluminescence intensity (Figure 1A). The improvement in photoluminescence intensity

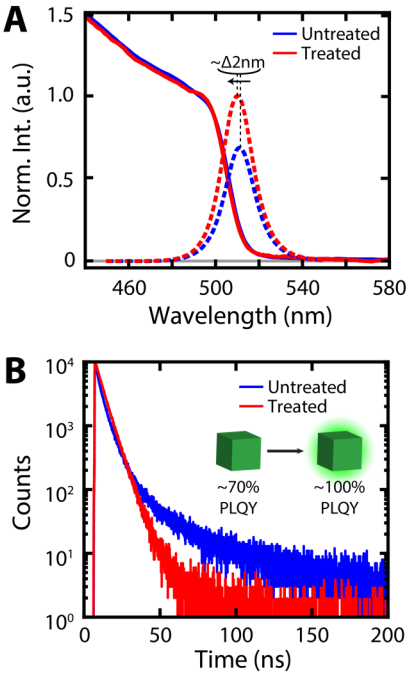

Figure 1: (A) Absorption (solid lines) and photoluminescence spectra (dotted lines) of a representative as-isolated ligand concentration CsPbBr3 nanocrystal sample dispersed in hexanes before treatment (blue lines) and after treatment (red lines) with ammonium thiocyanate. Photoluminescence spectra are normalized to the respective PLQY. (B) Time resolved photoluminescence lifetimes under pulsed 407.1 nm excitation at room temperature for an untreated CsPbBr3 sample (initially 70±2.5% quantum yield, blue line) and the same CsPbBr3 sample after treatment with thiocyanate (afterwards 100±2.5% quantum yield, red line).

and PLQY arises due to reduced non-radiative recombination, changing the excited state decay from multi-exponential to single-exponential (Figure 1B).

Conveniently, the stretch of the cyano- group has a characteristic vibrational frequency when bound to lead[45] (Supporting Information), providing an infrared handle to quantify the number of lead atoms removed during etching per particle. By monitoring the etching reaction with quantitative infrared spectroscopy, photoluminescence lifetime, and PLQY we can determine the number of under-coordinated lead atoms present throughout the etching which also informs us of the number of bromine vacancies present. For example, a sample that initially presents a 70% PLQY, Figure 1A/1B, contains nearly 90 bromine vacancies per nanocrystal (Supporting Information), a defect density of 10^{20} cm^{-3}. For this sample, we find that each under-coordinated lead atom in a 10 nm edge length $CsPbBr_3$ nanocrystal cube contributes 0.0006±0.0003 ns^{-1} (Supporting Information) to the overall non-radiative rate, a contribution 200 times smaller than the radiative rate. So, while an individual bromine vacancy is not severely detrimental to the overall PLQY, the culminative effect of many vacancies does significantly affect the overall optical performance of the material. It is also worth noting that a single such defect then could limit the quantum yield for luminescence to 0.995, close to the highest value that was recently measured for a CdSe/CdS colloidal quantum dot[10], and below the level of interest for some advanced energy harvesting applications. Further investigations into the composition dependent trapping dynamics and cross-sections of individual electronic defects are

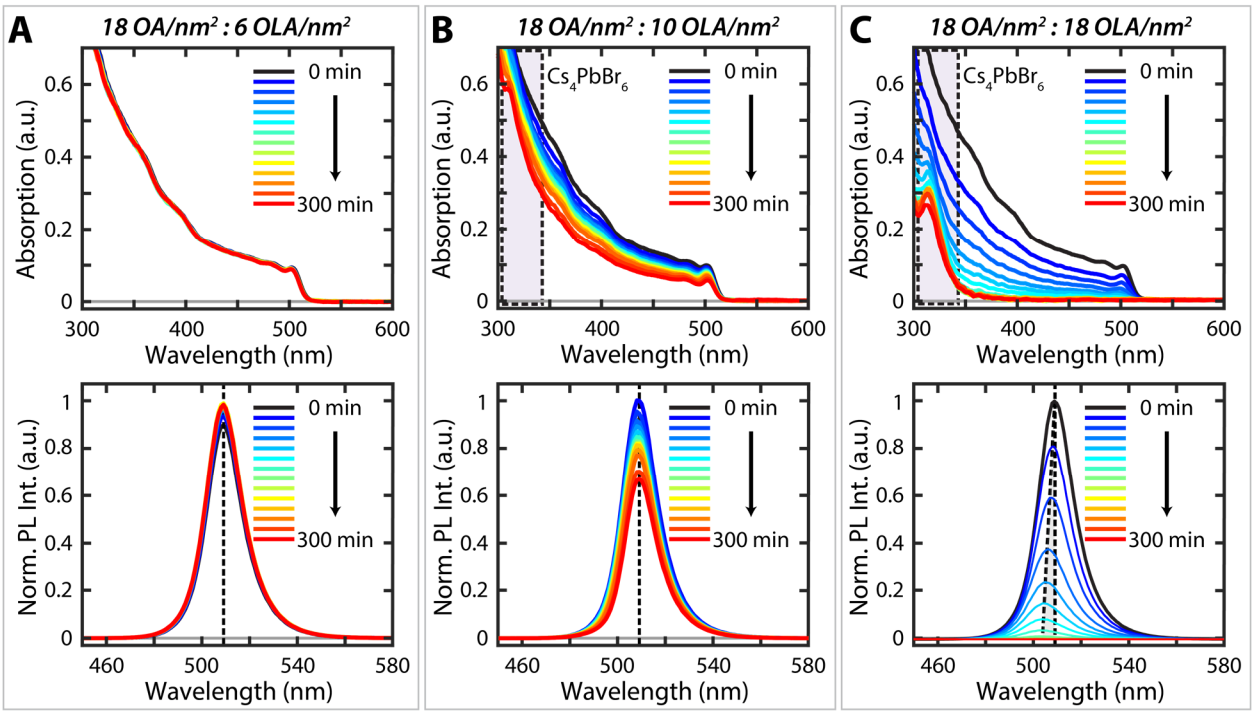

Figure 2: Evolution of the absorption and photoluminescence spectra of $CsPbBr_3$ samples throughout the thiocyanate etching reaction with varying ligand concentrations (time progressing from dark purple to red in each sub-figure): (A) 18 Oleic Acid and 6 Oleylamine ligands per square nanometer of nanocrystal surface area, (B) 18 Oleic Acid and 10 Oleylamine ligands per square nanometer of nanocrystal surface area, (C) 18 Oleic Acid and 18 Oleylamine ligands per square nanometer of nanocrystal surface area. Two spectroscopic regions of interest in the absorption spectra from (B) and (C) is the evolution of a characteristic peak near 313 nm related to the lead-depleted Cs_4PbBr_6 material, and the characteristic spectra of $CsPbBr_3$ as the etching reaction progresses. Also, of interest in the photoluminescence spectra of (A-C) is the systematic blue-shift of the bandgap of emissive $CsPbBr_3$ as the etching reaction progresses.

needed to fully understand the nature of defects in these materials, but are outside the scope of this work. By etching as-isolated $CsPbBr_3$ nanocrystals with thiocyanate, we can somewhat reliably improve the ensemble PLQY to near-unity (Figure 1A/1B). The conditions appear to allow the etchant to interact with a limited number of surface sites. However, given the weak nature of bonding in these materials, it is likely that there are necessary equilibria required to achieve the etching selectivity.

Long-chain hydrocarbon ligands not only play an important role in maintaining the ensemble colloidal properties but also drive many nanoscale post-synthetic transformations through relatively strong ligand interactions[46-49]. Therefore, it is important to consider the role ligand-thiocyanate salt interactions might play in dictating reaction outcomes. With two different ligands present in solution during the etching, oleic acid and oleylamine, we need to understand the relevance of the ligands separately, as well as the coincidence of both ligands. At the ligand concentrations used for our etching reactions, introducing only extra oleic acid or oleylamine does not increase the observed extent of etching when thiocyanate is added (Supporting Information) compared to as-isolated conditions. By systematically increasing the concentration of both ligands in solution, there are substantial changes to the observed etching trajectories (Figure 2A-C, Supporting Information). Instead of maintaining an unchanged absorption spectrum as seen for the as-isolated conditions (Figure 1A, 2A), we observe systematically larger decreases in $CsPbBr_3$ nanocrystals present while increasing the ligand concentration, as well as the appearance and growth of an absorption feature near 313 nm consistent with the lead-depleted phase[48-50], Cs_4PbBr_6 (Figure 2B, 2C). Conversion to Cs_4PbBr_6 has been shown to be possible by increasing the ligand concentration present[48-50], but at these conditions there is no etching or conversion observed without introducing thiocyanate (Supporting Information). This suggests that the concentration of oleate-oleylammonium ligand ion pairs present in solution have an important role in dictating the outcome of the etching reaction.

The thiocyanate etchant chemical potential that the $CsPbBr_3$ nanocrystals are exposed to is easily modulated by varying the oleate-oleylammonium ion pair concentration available in solution, dictating the amount of and rate that lead is removed from the nanocrystals (Figure 3A). Only 3% of the lead on average is etched per nanocrystal (Supporting Information) when exposed to as-isolated ligand concentrations (6 Oleic Acid: 6 Oleylamine per nm^2, Figure 3A, dark blue). However, with higher ligand ion-pair concentrations (18 Oleic Acid: 18 Oleylamine per nm^2) present in solution (Figure 3A, red), the entire $CsPbBr_3$ ensemble is converted to the lead depleted phase after one hour, requiring nearly 75% of the lead from the nanocrystal to be removed. Although the extent and rate of lead etching can be varied substantially by modulating the oleate-oleylammonium ion pair concentration, the ensemble is still able to reach near-unity PLQYs through etching (Figure 3B, color coordinated with the curves in Figure 3A). This shows that over a range of etchant chemical potentials some etching selectivity is maintained, removing under-coordinated lead atoms more quickly than fully coordinated lead atoms. But, by increasing the etchant chemical potential the degree of selectivity is reduced (Supporting Information), requiring more lead to be removed overall from the nanocrystal before reducing the number of optically deleterious lead atoms and improving the ensemble PLQY. The change in selectivity is most apparent in the highest chemical potential

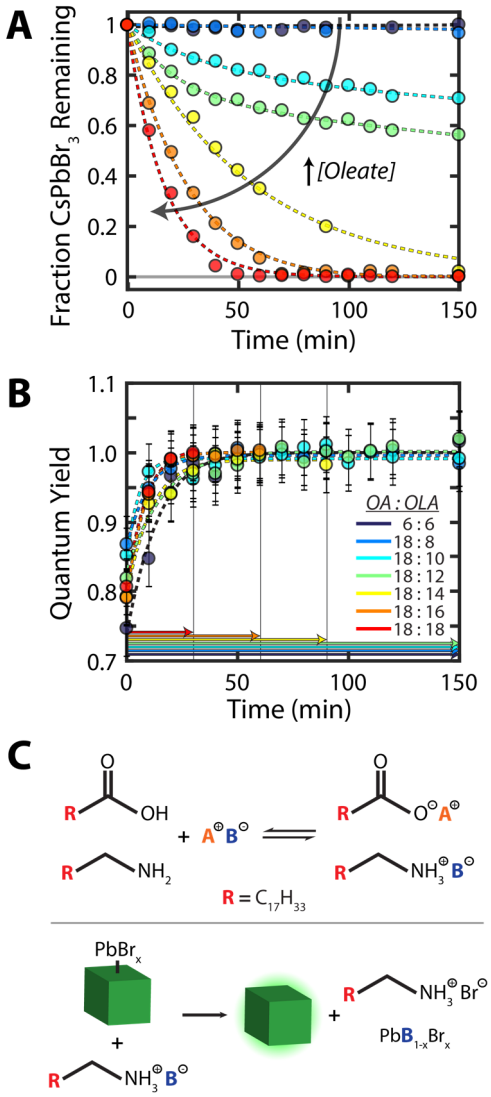

Figure 3: (A) Fraction of $CsPbBr_3$ remaining in solution relative to the initial concentration present throughout the thiocyanate etching reaction conducted at varying oleylammonium-oleate ion pair concentrations present in solution, with the arrow showing increasing concentration for clarity (ligand concentrations are color coordinated with values appearing in Figure 3B). (B) Change in the $CsPbBr_3$ ensemble quantum yield as etching progresses. Arrows and vertical lines indicate when the sample absorption decreased too far to accurately measure the quantum yield of the sample. (C) From etching reactions conducted at different conditions (Figure 3A/3B, SI), we propose the equilibrium of sample ligands and added ionic thiocyanate salts create the active etching species which is able to remove lead from the nanocrystal.

presented in Figure 3A/3B (red line), in which the ensemble PLQY is just able to reach near-unity before it fully converts to the lead-depleted phase.

Despite previous notions, thiocyanate does not intrinsically possess a conveniently tuned binding strength to lead, but instead the selectivity arises from finely tuning the etchant chemical potential. For this reaction the concentration of etchant present in solution is critically controlled by an equilibrium between the ionic thiocyanate salts and the oleate-oleylammonium ion pairs present (Figure 3C), affording the ability to finely tune the etchant chemical potential. The emergence of characteristic signatures of the thiocyanate counter-ion coordinated to oleate are readily observed with IR spectroscopy (Supporting Information). Solubilized thiocyanate ions can then diffuse to the nanoparticle surface and remove lead (Figure 3C). This removal of under-coordinated lead is what ultimately improves the ensemble PLQYs, consistent with previous reports[12,14,15]. While we measure concentrations of 6 Oleic Acid: 6 Oleylamine per nm^2 from NMR of as-isolated nanocrystals (Supporting Information), based on the observed extent of etching only a fraction, around 5% (Supporting Information), are available as oleate-oleylammonium ion pairs while the remainder are likely already surface ligands or coordinated with ions left over from the synthesis. Depending on the synthesis stoichiometry employed and the subsequent cleaning steps, there may be too few oleate-oleylammonium ion pairs present to solubilize enough thiocyanate to remove all the under-coordinated lead present. This limitation puts an upper bound on the achievable PLQY following etching, explaining why some samples only achieve modest improvements. However, introducing additional small quantities of ligand ion pairs into solution can increase the etchant concentration in a controlled manner, controllably achieving near-unity PLQYs (Supporting Information). Moreover, since ligands are consumed during the etching reaction (Figure 3C), nanocrystals tend to aggregate and lose colloidal stability throughout the etching if there are too few ligands present in solution (Supporting Information). This ability to dictate the extent of etching allows for precise control of the etching reaction, removing just enough lead atoms to reach near-unity PLQYs without etching too many atoms from the nanocrystal (Supporting Information).

While the underlying chemical reactions dictate the rate at which particular lead species are removed, they do not inform spatially where within the nanocrystal the lead is preferentially removed from during the etching. With low concentrations of etchant present changes to the shape and size of the nanocrystal ensemble are negligible (Supporting Information), consistent with the small quantity of lead removed from the nanocrystal. By increasing the etchant concentration present in solution (in turn achieved by increasing the ligand ion-pair concentration) (Figure 4A), the $CsPbBr_3$ nanocrystals become significantly more uniform throughout the etching reaction, presenting a more consistent and regular cube-like morphology. This is a significant specific advantage to this controlled etching method. In addition to increased particle uniformity, the average feret diameter of the ensemble systematically decreases and narrows, by around 15%, as the etching reaction progresses with higher etchant concentrations (Figure 4B). A systematic blue-shift of the bandgap arises from the change in average size of the ensemble, whereas the narrowing of the size distribution and photoluminescence spectrum arises from a size-dependent etching rate (Supporting Information), in which larger particles etch at faster rates than smaller particles. These observations also add a valuable insight towards the bandgap blue-shifts that arise following similar $CsPbBr_3$ treatments in the literature[12,14,15,48-50], with observed shifts ranging from 1 nm to 5 nm. While we are not able to conclusively rule out the role of ligands coupling to the electronic states of the nanocrystal, a decrease in size and size distribution narrowing offers simple explanations for the observed bandgap blue-shift with increasingly aggressive etching conditions (Figure 2A-C, Supporting Information).

The change in nanocrystal uniformity and commensurate increase in PLQY as a result of etching suggests the order and

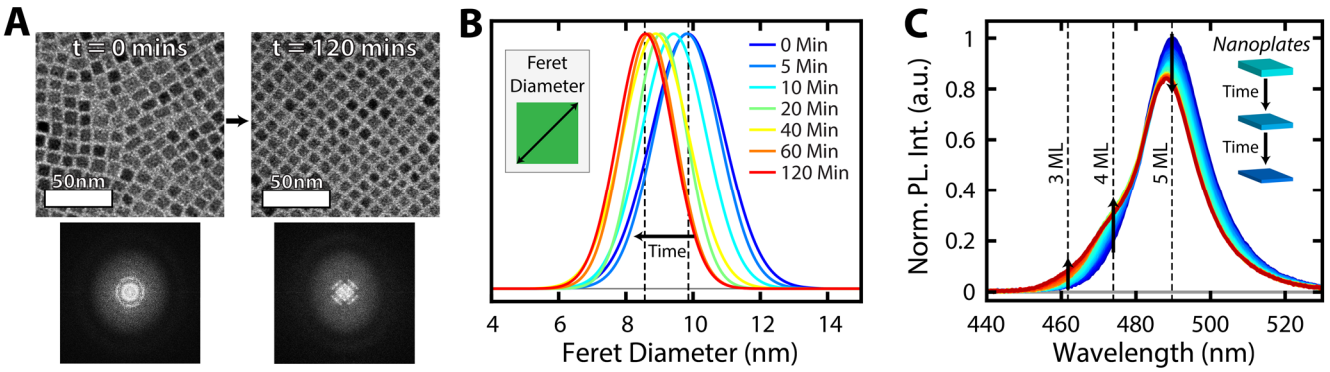

Figure 4: Changes in the nanocrystal structure as the thiocyanate etching reaction progresses. (A) TEM micrographs of $CsPbBr_3$ nanocrystal cubes showing the change in morphology following thiocyanate treatment (0 minutes and 120 minutes) with 18 Oleic Acid and 16 Oleylamine ligands per square nanometer of $CsPbBr_3$ nanocrystal surface area, scale bar represents 50 nm. Also shown are FFT of the TEM images, highlighting the change in sample uniformity following treatment. (B) For the etching reaction of $CsPbBr_3$ nanocrystal cubes shown in Figure 4A, the time evolution of the cube feret diameter distribution with etching, with time progressing from dark blue to red. (C) Evolution of the photoluminescence spectra of $CsPbBr_3$ nanoplates as thiocyanate etching progresses, beginning with a characteristic 488 nm photoluminescence peak and proceeding with the sequential growth of both 477 nm and 462 nm photoluminescence components with time (time progressing from dark blue to red) (Supporting Information).

location in which lead is removed from the nanocrystal surface. Instead of proceeding by randomly removing lead atoms, under-coordinated lead atoms are etched more quickly and then the etching proceeds by sequentially removing layers of perovskite, at least for the chemical potentials shown in Figure 3A/3B. This trajectory is consistent with a layer-by-layer etching mechanism in which layers that are already partially etched etch at a faster rate than removing material from the next complete layer below[39,51,52]. The observed improvements in both uniformity and PLQY for the range of chemical potentials in Figure 3A/3B are inconsistent with a randomly proceeding etching reaction. Fortunately, this microscopic etching mechanism can be tested by monitoring the etching trajectories of quasi-2D $CsPbBr_3$ nanoplates. The discrete nature of bandgap energies that arise from 2D quantum confinement act as a direct reporter of the nanoplate thickness[53,54] (488, 477, 462, 435, and 405 nm for 5-, 4-, 3-, 2-, and 1-monolayer thicknesses respectively), presenting a convenient handle to monitor the etching progression. Starting with a 5-monolayer $CsPbBr_3$ nanoplate (Figure 4C, Supporting Information), we observe a decrease in the 5-monolayer intensity while subsequently observing a peak appear at 477 nm (4-monolayer thick sub-population) and then later a peak at 462 nm (3-monolayer thick subpopulation). The sequential appearance of thinner nanoplate subpopulations as thicker nanoplates etch is highly consistent with a layer-by-layer etching mechanism, showing an underlying well-ordered etching sequence.

Although our work highlights the underlying mechanism of thiocyanate-based etching, we find that the observed selective etching does not arise from unique properties of thiocyanate. Instead this method can be applied generally using other controlled chemical etchants. The critical factor is the etchant chemical potential which can be tuned by not only changing the etchant concentration, but also by modulating the strength of the etchant-etched atom interaction. The strength of this interaction is determined by the electron density[55] present on the atom that binds to lead which changes the etchant hardness (Figure 5A). By varying etchant hardness, with tetramethylthiourea being the softest species tested and octanedithiol being the hardest, we observe substantial changes in the rate of etching under similar concentrations in accordance with their respective chemical potentials (Figure 5A). Consistent with previous reports, the addition of hard etchants such as thiols[48,50], results in rapid etching of $CsPbBr_3$ culminating in conversion to the lead-depleted phase material. By systematically varying the etchant chemical potential, we identify three general etching regimes (Figure 5A): improvement of the quantum yield (green shading), modest if any change in the quantum yield (yellow shading), and deterioration of the quantum yield (red shading). Expectedly, further increasing the thiocyanate etchant chemical potential beyond that presented in Figure 3A/3B results in a gradual transition from beneficial to neutral to detrimental (Figure 5B). At first, the etching reaction becomes less selective, increasing the number of lead atoms that need to be removed before reducing the population of under-coordinated lead atoms present, systematically shifting the achievable PLQY lower as the etchant chemical potential is increased (Figure 5B). Continuing to increase the etchant chemical potential further causes the etching to transition into a non-selective and detrimental region (Figure 5B, cyan to dark blue), removing lead atoms from the nanocrystal without regard for their local chemical environment, which decreases the ensemble PLQY. The transition from selective to non-selective etching is analogous to the roughening transitions observed in other systems[39,58,59], in which atoms are randomly removed from multiple layers as they are encountered. While there are some advantages to operating in high etchant chemical potential regions, such as short reaction times and a wider library of useable etchants, there are substantial tradeoffs in etching selectivity and achievable optical efficiencies that must be carefully considered.

This method significantly increases the library of useable chemicals, particularly for those with strong binding strengths with lead, by carefully controlling the concentration of etchant present in solution at any given time. By slowly introducing a hard-chemical etchant like thiol into solution, the etchant chemical potential is maintained as low as possible for that species, representing perhaps the best-case scenario for introducing hard-chemical etchants. Instead of observing a rapid degradation of the optical properties, by slowly adding octanedithiol to the solution, the ensemble PLQY improves from 60% to nearly 85% (Figure 5C). Although the library of chemical etchants to

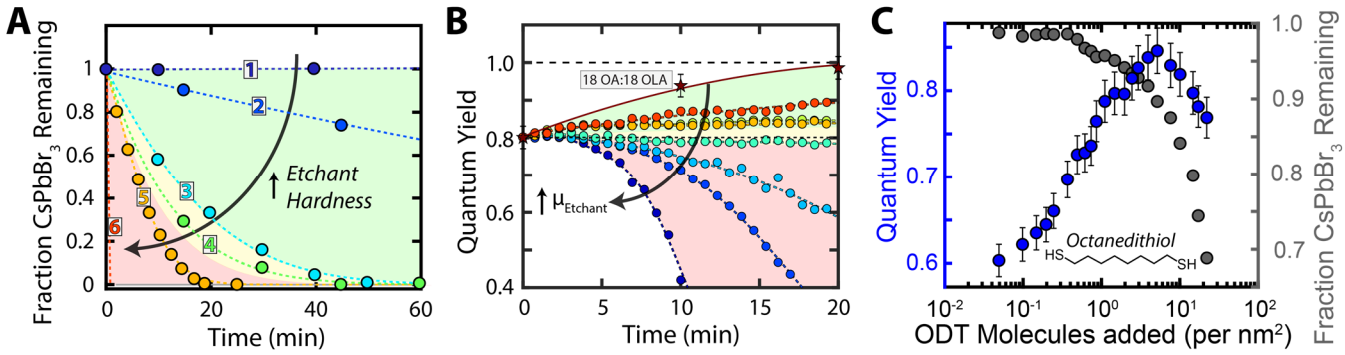

Figure 5: (A) Change in the etching rate of $CsPbBr_3$ nanocrystal cubes by changing the hardness of the chemical etchant introduced, (1, Tetramethylthiourea. 2, Potassium Selenocyanate. 3, Ammonium Thiocyanate., 4, Potassium Thioacetate., 5, Sodium Diethyldithiocarbamate., 6, Octanedithiol.) depicted as the fraction of $CsPbBr_3$ remaining in solution as the etching reaction progresses. Each etching reaction was conducted with 18 Oleic Acid: 18 Oleylamine ligands per nm^2, which introduces the same concentration of etchant into solution. Background highlighting distinguishes regions of quantum yield improvement (green), no change or subtle quantum yield improvement (yellow), and detrimental to quantum yield (red). (B) Progression of quantum yield during thiocyanate etching conducted at different chemical potentials of thiocyanate etchant, ranging from 18 Oleic Acid:18 Oleylamine (dark red stars) to 50 Oleic Acid:50 Oleylamine (dark blue circles) ligands per nm^2. (C) Change in $CsPbBr_3$ nanocrystal cube ensemble quantum yield by slowly introducing octanedithiol (ODT) into solution, a hard-chemical etchant for lead in $CsPbBr_3$ nanocrystals.

improve PLQY is slightly expanded through slow-addition of the etchant, achieving near-unity PLQYs with excessively hard-chemical etchants is either more difficult or in some cases intractable as the etchant chemical potential is still too high even at modest concentrations at room temperature to achieve high levels of selectivity. This ultimately shows that many of the chemical strategies that were developed to post-synthetically manipulate metal chalcogenide materials[58-60] are partially, if not completely, incompatible with lead halide perovskites. The chemicals that were employed are too aggressive for the weakly bound lead halide perovskite materials. Therefore, while the post-synthetic techniques may be analogous, careful optimizations of chemical strengths and concentrations are necessary to avoid undesirable outcomes and unintended side reactions.

Conclusions

The cesium lead halide perovskites present a promising emerging platform for developing a new generation of near-unity PLQY nanocrystal luminophores throughout the visible. While the weak internal bonding certainly presents substantial challenges – poor photostability, poor chemical stability, low melting point, and facile formation of defects – it also offers tremendous opportunities to perform selective post-synthetic treatments under mild and tunable conditions at room temperature. Post-synthetic etching represents a convenient path for mitigating the presence and optoelectronic consequences of bromine vacancies and under-coordinated lead atoms within the lead halide perovskites. To better control the post-synthetic selective etching in $CsPbBr_3$ nanocrystals, we set out to improve our understanding of the thiocyanate-based etching mechanism. By changing the etchant chemical potential, either with concentration or strength of the chemical etchant, we systematically vary the extent of etching from removing only a few lead atoms to nearly all the lead atoms of the nanocrystal. The etching is not able to remove enough under-coordinated lead atoms to reach near-unity PLQYs when the chemical potential is too low. When the chemical potential is too high the etching reaction becomes non-selective. Only by selecting a chemical etchant with an appropriate lead binding strength and concentration, is it possible to selectively target under-coordinated lead atoms on the surface of $CsPbBr_3$ nanocrystals, reliably improving the PLQY. From our studies we show that thiocyanate is not a unique chemical etchant but instead is one member of a larger family of chemical etchants. The critical property for selective etching is the etchant chemical potential. Although we focus on $CsPbBr_3$, this study presents a rational framework for systematically improving the optical quality of other lead halide perovskite compositions, opening paths for reliably obtaining perovskite near-unity emitters throughout the visible. By developing robust chemical strategies to access materials at the high radiative efficiency limit, future investigations into promising optoelectronic applications operating at the upper efficiency limits are possible.

ASSOCIATED CONTENT

Supporting Information. The supporting information is available free of charge on the ACS Publications Website at DOI:

Synthetic methods, sample characterization, additional supporting figures (PDF)

AUTHOR INFORMATION

Corresponding Author.
*E-mail: paul.alivisatos@berkeley.edu

ORCID

Author Contributions

The manuscript was written and reviewed by all authors. All authors have given approval of the final version of this manuscript.

Notes

The authors declare no competing financial interest.

ACKNOWLEDGMENT

This work was supported by the U.S. Department of Energy, Office of Science, Office of Basic Energy Sciences, Materials Sciences and Engineering Division, under Contract No. DE-AC02-05-CH11231 within the Physical Chemistry of Inorganic Nanostructures Program (KC3103). The authors would also like to thank Joseph Swabeck, David Hanifi, David Nenon, Matthew Hauwiller, and Nima Balan for insightful discussions or reviewing the manuscript.

REFERENCES

1. Lim, J., Park, Y., Wu, K., Yun, H.J., Klimov, V.I., *Nano Lett.*, 2018, 18, 6645
2. Caruge, J.M., Halpert, J.E., Wood, V., Bulović, Bawendi, M.G., *Nature Photonics*, 2008, 2, 247
3. Lee, S., Kim, D.B., Yu, J.C., Jang, C.H., Park, J.H., Lee, B.R., Song, M.H., *Adv. Mater.*, 2019, 1805244
4. Li, Y., Shi, Z., Li, S., Lei, L., Ji, H., Wu, D., Xu, T., Tian, Y., Li, X., *J. Mater. Chem. C*, 2017, 5, 8355
5. Ramasamy, P., Lim, D., Kim, B., Lee, S., Lee, M., Lee, J., *Chem. Commun.*, 2016, 52, 2067
6. Braly, I.L., deQuilettes, D.W., Pazos-Outón, L.M., Burke, S., Ziffer, M.E., Ginger, D.S., Hillhouse, H.W., *Nature Photonics*, 2018, 12, 355
7. Miller, O.D., Yablonovitch, E., Kurtz, S.R., *IEEE J. Photovoltaics*, 2012, 2, 303
8. Needell, D.R., Ilic, O., Bukowsky, C.R., Nett, Z., Xu, L., He, J., Bauser, H., Lee, B.G., Geisz, J.F., Nuzzo, R.G., Alivisatos, A.P., Atwater, H.A., *IEEE J. Photovoltaics*, 2018, 8, 1560
9. Sanehira, E.M., Marshall, A.R., Christmas, J.A., Harvey, S.P., Ciesielski, P.N., Wheeler, L.M., Schulz, P., Lin, L.Y., Beard, M.C., Luther, J.M., *Sci. Adv.*, 2017, 3:eaao4204
10. Hanifi, D.A., Bronstein, N.D., Koscher, B.A., Nett, Z., Swabeck, J.K., Takano, K., Schwartzberg, A.M., Maserati, L., Vandewal, K., van de Burgt, Y., Salleo, A., Alivisatos, A.P., 2019, *In Press*
11. Chen, O., Zhao, J., Chauhan, V.P., Cui, J., Wong, C., Harris, D.K., Wei, H., Han, H., Fukumura, D., Jain, R.K., Bawendi, M.G., *Nature Materials*, 2013, 12, 445
12. Nenon, D.P., Pressler, K., Jang, J., Koscher, B.A., Olshansky, J.H., Osowiecki, W.T., Koc, M.A., Wang, L., Alivisatos, A.P., *J. Am. Chem. Soc.,* 2018, 140, 17760
13. Stasio, F.D., Christodoulou, S., Huo, N., Konstantatos, G., *Chem. Mater.*, 2017, 29, 7663
14. Ahmed, T., Seth, S., Samanta, A., *Chem. Mater.*, 2018, 30, 3633
15. Koscher, B.A., Swabeck, J.K., Bronstein, N.D., Alivisatos, A.P., *J. Am. Chem. Soc.*, 2017, 139, 6566
16. Protesescu, L., Yakunin, S., Bodnarchuk, M.I., Krieg, F., Caputo, R., Hendon, C.H., Yang, R.X., Walsh, A., Kovalenko, M.V., *Nano Lett.*, 2015, 15, 3692
17. Imran, M., Caligiuri, V., Wang, M., Goldoni, L., Prato, M., Krahne, R., Trizio, L.D., Manna, L., *J. Am. Chem. Soc.,* 2018, 140, 2656
18. Amgar, D., Aharon, S., Etgar, L., *Adv. Funct. Mater.*, 2016, 26, 8576
19. Manser, J.S., Christmas, J.A., Kamat, P.V., *Chem. Rev.*, 2016, 116, 12956
20. Moyen, E., Jun, H., Kim, H., Jang, J., *ACS Appl. Mater. Interfaces*, 2018, 42647
21. Lee, S., Kim, D.B., Yu, J.C., Jang, C.H., Park, J.H., Lee, B.R., Song, M.H., *Adv. Mater.*, 2019, 1805244
22. Tan, Y., Zou, Y., Wu, L., Huang, Q., Yang, D., Chen, M., Ban, M., Wu, C., Wu, T., Bai, S., Song, T., Zhang, Q., Sun, B., *ACS Appl. Mater. Interfaces*, 2018, 10, 3784
23. Yakunin, S., Protesescu, L., Krieg, F., Bodnarchuk, M.I., Nedelcu, G., Humer, M., Luca, G.D., Fiebig, M., Heiss, W., Kovalenko, M.V., *Nature Comm.* 2015, 6, 8056
24. Hu, F., Zhang, H., Sun, C., Yin, C., Lv, B., Zhang, C., Yu, W.W., Wang, X., Zhang, Y., Xiao, M., *ACS Nano* 2015, 9, 12410
25. Raino, G., Nedelcu, G., Protesescu, L., Bodnarchuk, M.I., Kovalenko, M.V., Mahrt, R.F., Stőferle, T., *ACS Nano* 2016, 10, 2485
26. Becker, M.A., Scarpelli, L., Nedelcu, G., Raino, G., Masia, F., Borri, P., Stoferle, T., Kovalenko, M.V., Langbein, W., Mahrt, R.F., *Nano Lett.*, 2018, 18, 7546
27. Raino, G., Becker, M.A., Bodnarchuk, M.I., Mahrt, R.F., Kovalenko, M.V., Stőferle, T., *Nature*, 2018, 563, 671
28. Kang, J., Wang, L., *J. Phys. Chem. Lett.*, 2017, 8, 489
29. Giansante, C., Infante, I., *J. Phys. Chem. Lett.*, 2017, 8, 5209
30. Bodnarchuk, M.I., Boehme, S.C., ten Brinck, S., Bernasconi, C., Shynkarenko, Y., Krieg, F., Widmer, R., Aeschlimann, B., Gunther, D., Kovalenko, M.V., Infante, I., *ACS Energy Lett.*, 2019, 4, 63
31. Buin, P., Pietsch, P., Xu, J., Voznyy, O., Ip, A.H., Comin, R., Sargent, E.H., *Nano Lett.*, 2014, 14, 6281
32. Leguy, A.M.A., Frost, J.M., McMahon, A.P., Sakai, V.G., Kockelmann, W., Law, C., Li, X., Foglia, F., Walsh, A., O'Regan, B.C., Nelson, J., Cabral, J.T., Barnes, P.R.F., *Nature Comm.*, 2015, 6, 7124
33. Yuan, Y., Huang, J., *Acc. Chem. Res.*, 2016, 49, 286
34. Mosconi, E., Angelis, F.D., *ACS Energy Lett.*, 2016, 1, 182
35. De Roo, J., Ibanez, M., Geiregat, P., Nedelcu, G., Walravens, W., Maes, J., Martins, J.C., Driessche, I.V., Kovalenko, M.V., Hens, Z., *ACS Nano*, 2016, 10, 2071
36. Krieg, F., Ochsenbein, S.T., Yakunin, S., ten Brinck, S., Aellen, P., Suess, A., Clerc, B., Guggisberg, D., Nazarenko, O., Shynkarenko, Y., Kumar, S., Shih, C., Infante, I., Kovalenko, M.V., *ACS Energy Lett.*, 2018, 641
37. Pan, J., Quan, L., Zhao, Y., Peng, W., Murali, B., Sarmah, S. P., Yuan, M., Sinatra, L., Alyami, N. M., Liu, J., Yassitepe, E., Yang, Z., Voznyy, O., Comin, R., Hedhili, M. N., Mohammed, O. F., Lu, Z. H., Kim, D., Sargent, E. H., Bakr, O. M., *Adv. Mater.,* 2016, 28, 8718-8725
38. Hauwiller, M.R., Frechette, L.B., Jones, M.R., Ondry, J.C., Rotskoff, G.M., Geissler, P., Alivisatos, A.P., *Nano Lett.*, 2018, 18, 5731
39. Ye, X., Jones, M. R., Frechette, L. B., Chen, Q., Powers, A. S., Ercius, P., Dunn, G., Rotskoff, G. M., Nguyen, S. C., Adiga, V. P., Zettl, A., Rabani, E., Geissler, P.L., Alivisatos, A.P., *Science* 2016, 354, 874
40. Yablonovitch, E., Gmitter, T., Harbison, J.P., Bhat, R., *Appl. Phys. Lett.*, 1987, 51, 2222
41. Yoon, J., Jo, S., Chun, I.S., Jung, I., Kim, H., Meitl, M., Menard, E., Li, X., Coleman, J.J., Paik, U., Rogers, J.A., *Nature*, 2010, 465, 329
42. Liu, L., Peng, Q., Li, Y., *Inorg. Chem.*, 2008, 47, 3182
43. Khon, E., Lambright, K., Khnayzer, R.S., Moroz, P., Pepera, D., Butaeva, E., Lambright, S., Castellano, F.N., Zamkov, M., *Nano Lett.*, 2013, 13, 2016
44. Micic, O.I., Sprague, J., Lu, Z., Nozik, A.J., *Appl. Phys. Lett.*, 1996, 68, 3150
45. Fafarman, A.T., Koh, W., Diroll, B.T., Kim, D.K., Ko, D., Oh, S.J., Ye, X., Doan-Nguyen, V., Crump, M.R., Reifsnyder, D.C., Murray, C.B., Kagan, C.R., *J. Am. Chem. Soc.*, 2011, 133, 15753
46. Dong, C., van Veggel, C.J.M., *ACS Nano*, 2009, 3, 123
47. Boles, M.A., Ling, D., Hyeon, T., Talapin, D.V., *Nature Materials*, 2016, 15, 141
48. Liu, Z., Bekenstein, Y., Ye, X., Nguyen, S.C., Swabeck, J., Zhang, D., Lee, S., Yang, P., Ma, W., Alivisatos, A.P., *J. Am. Chem. Soc.*, 2017, 139, 5309
49. Udayabhaskararao, T., Houben, L., Cohen, H., Menahem, M., Pinkas, I., Avram, L., Wolf, T., Teitelboim, A., Leskes, M., Yaffe, O., Oron, D., Kazes, M., *Chem. Mater.*, 2018, 84
50. Wu, L., Hu, H., Xu, Y., Jiang, S., Chen, M., Zhong, Q., Yang, D., Liu, Q., Zhao, Y., Sun, B., Zhang, Q., Yin, Y., *Nano Lett.*, 2017, 17, 5799
51. Aoyagi, Y., Shinmura, K., Kawasaki, K., Tanaka, T., Gamo, K., Namba, S., Nakamoto, I., *Appl. Phys. Lett.*, 1992, 60, 968
52. Parkinson, B., *J. Am. Chem. Soc.*, 1990, 112, 7498
53. Akkerman, Q.A., Motti, S.G., Kandada, A.R.S., Mosconi, E., D'Innocenzo, V., Bertoni, G., Marras, S., Kamino, B.A., Miranda, L., Angelis, F.D., Petrozza, A., Prato, M., Manna, L., *J. Am. Chem. Soc.*, 2016, 138, 1010
54. Bekenstein, Y., Koscher, B.A., Eaton, S.W., Yang, P., Alivisatos, A.P., *J. Am. Chem. Soc.*, 2015, 137, 16008
55. Pearson, R.G., *J. Chem. Educ.*, 1968. 45, 9, 581
56. Vlachos, D.G., Schmidt, L.D., Aris, R., *Phys. Rev. B*, 1993, 47, 4896
57. Lam, R., Vlachos, D.G., *Phys. Rev. B*, 2001, 64, 035401
58. Dong, A., Ye, X., Chen, J., Kang, Y., Gordon, T., Kikkawa, J.M., Murray, C.B., *J. Am. Chem. Soc.*, 2011, 133, 998
59. Brown, P.R., Kim, D., Lunt, R.B., Zhao, N., Bawendi, M.G., Grossman, J.C., Bulovic, V., *ACS Nano*, 2014, 8, 5863
60. Kagan, C.R., Murray, C.B., *Nature Nano.,* 2015, 10, 1013

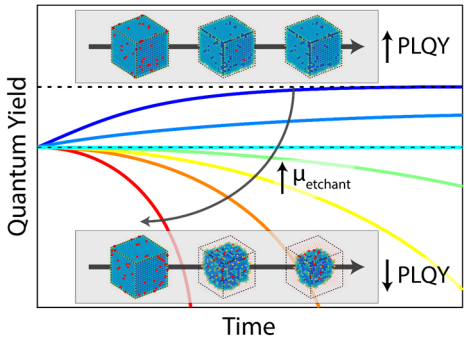
PLQY
Quantum Yield
μetchant
PLQY
Time

Supporting Information for:

Investigation of the underlying chemical mechanism of highly selective cesium lead bromide nanocrystals for reliably accessing near-unity emitters

Brent A. Koscher[1,3,4], Zach Nett[1,3,4], and A. Paul Alivisatos[1,2,3,4]

[1] Department of Chemistry, University of California, Berkeley, CA 94720, USA.
[2] Department of Materials Science and Engineering, University of California, Berkeley, CA 94720, USA.
[3] Materials Science Division, Lawrence Berkeley National Laboratory, Berkeley, CA 94720, USA.
[4] Kavli Energy NanoScience Institute, Berkeley, CA 94720, USA.

Materials: Cesium carbonate (Cs_2CO_3, 99.9%, Aldrich), octadecene (ODE, 90%, Aldrich), oleic acid (OA, 90%, Aldrich), oleylamine (OLA, 70%, Aldrich), lead bromide ($PbBr_2$, 99.999%, Aldrich), hexanes (>99%, Aldrich, anhydrous), toluene (99.8%, Aldrich, anhydrous), ethyl acetate (99.8%, Aldrich, anhydrous), ammonium thiocyanate (NH_4SCN, 99.99%, Aldrich), sodium thiocyanate (NaSCN, 99.99%, Aldrich), lead thiocyanate (99.5%, Aldrich), octanedithiol (>97%, Aldrich), sodium diethyldithiocarbamate (>99%, Aldrich), potassium thioacetate (98%, Aldrich), potassium selenocyanate (>99%, Aldrich), tetramethylthiourea (98%, Aldrich)

Synthetic Methods:

Preparation of Cesium Oleate Stock Solution

A stock solution of cesium oleate was prepared following the reported procedure by Protesescu *et al.* (Ref 16). Briefly, 2.5 mmol Cs_2CO_3 and 2.5 mL OA was loaded into a three-neck flask containing 40 mL ODE. The mixture was dried/degassed for 1 hour at 120 °C under high vacuum, then heated under dry Argon gas at 150 °C until all the Cs_2CO_3 complexed with OA.

Preparation of Ligands for Synthesis

Small quantities of OA and OLA (typically on the 5-10 mL scale) were prepared ahead of time for use in the synthesis. The technical grade OA and OLA liquids were filtered through a PTFE syringe filter to remove any large floating particulates and then loaded into separate glass vials. Then OA and OLA were dried/degassed for 1 hour at 120 °C and then transferred air-free into an argon glovebox for storage. Afterwards the OA and OLA were used without further processing.

Synthesis of $CsPbBr_3$ Nanocrystal Cubes

First ODE (5 mL) and $PbBr_2$ (0.188 mmol) were added into a three-neck flask, then dried/degassed under vacuum at 120 °C for 1 hour. Afterwards the reaction was heated under dry argon gas to 140 °C, at which point previously prepared OA (0.5 mL) and OLA (0.65 mL) were injected into the flask to complex the $PbBr_2$ salt. Following the complete dissolution of the $PbBr_2$ salt, the reaction temperature was adjusted between 140-160 °C before hot cesium oleate solution (0.5 mL, 0.125 M) was injected. The size of the obtained particles is modulated by changing the reaction temperature. After growing for 5-10 seconds, the reaction mixture was cooled close to room-temperature using an ice-water bath.

Isolation and Purification of $CsPbBr_3$ Nanocrystal Cubes

Three isolation methods work to good effect for 7-10 nm edge length $CsPbBr_3$ nanocrystal cube samples. In the first method, the crude reaction mixture was first centrifuged at 2000 RCF for 3 minutes to remove aggregates and other undesirably large by-products, then centrifuged at 11000 RCF for up to 10 minutes at low temperatures (0-10 °C), before finally re-dispersing the isolated particles in anhydrous hexanes for storage. In the second method, the crude solution was first centrifuged at 2000 RCF for 3 minutes to remove unwanted by-products, before adding ethyl acetate (or similar anti-solvent), centrifuging the resulting suspension at 9000 RCF for up to 10 minutes, and finally re-dispersing the isolated particles in anhydrous

hexanes for storage. In the third method, around 5 mL of hexanes were added to the crude reaction mixture and centrifuged at 2000 RCF to remove unwanted by-products. Next, hexanes were evaporated from the mixture in a step-wise fashion in order to isolate different size particles from the reaction solution by centrifugation at 9000 RCF for up to 10 minutes, and then the isolated particles were re-dispersed in anhydrous hexanes for storage. Each method results in long-term stable particles that can be stored in an inert atmosphere glovebox or in air, depending on the timeframe in which the samples were used.

Synthesis of $CsPbBr_3$ Nanocrystal Plates
First ODE (5 mL) and $PbBr_2$ (0.188 mmol) were added into a three-neck flask, then dried/degassed under vacuum at 120 °C for 1 hour. Afterwards the reaction was heated under dry argon gas to 140 °C, at which point previously prepared OA (0.5 mL) and OLA (0.5 mL) were injected into the flask to complex the $PbBr_2$ salt. Following the complete dissolution of the $PbBr_2$ salt, the reaction temperature was adjusted between 90-130 °C before hot cesium oleate solution (0.4 mL, 0.125 M) was injected. The size of the obtained particles is modulated by changing the reaction temperature. After growing for 5-10 seconds, the reaction mixture was cooled close to room-temperature using an ice-water bath.

Isolation and Purification of $CsPbBr_3$ Nanocrystal Plates
To isolate the nanocrystal plates, the reaction mixture was centrifuged at 9000 RCF for up to 10 minutes to yield a precipitate that was re-dispersed in hexanes. Decreasing the temperature during centrifugation can further help with isolation but is often not necessary for nanocrystal plates due to their larger volume. The nanocrystal plate samples were stored inside the glovebox or in air, depending on the timeframe in which the samples were used.

Characterization:
Absorption
Steady-state absorption spectra were collected using a Shimadzu UV-3600 double beam spectrometer set to the second slowest scanning rate, with one second integration and 2 nm slit widths.

Steady-state Fluorescence
For samples that produced measurable changes on the minutes time scale, steady-state fluorescence spectra were collected using a Horiba Jobin-Yvon FluoroLog 2 spectrofluorometer (wavelength calibration to the 397 nm Raman peak under 350 nm excitation to within 1 nm accuracy). Samples were excited by monochromatic light from a cold white ThorLabs LED passed through a monochromator (typical integration times of 0.2 s/nm with 1 nm slit widths were used).

For samples that produced measurable changes on faster time scales (seconds), steady-state fluorescence spectra were collected using a fiber-coupled, calibrated Ocean Optics USB2000 CCD spectrometer (wavelength calibrated to atomic lines from a Hg and Ne calibration lamp, spectral sensitivity calibrated using a radiometrically calibrated blackbody source from Ocean Optics). Samples were excited by a ThorLabs UV LED. Using the Ocean Optics CCD spectrometer, full spectra are typically collected in 0.1 s, and several are averaged together. Although spectra can be collected quickly, the CCD is less sensitive than the scanning PMT, representing a trade-off.

Additionally, some steady-state fluorescence spectra were collected using a home built integrating sphere spectrofluorometer with a Princeton Instruments Si-CCD, the setup is described further in the Quantum Yield Measurements Section.

Quantum Yield Measurements (PLQY)
A home-built integrating sphere spectrofluorometer was used to measure absolute quantum yields. A Fianium SC450 supercontinuum pulsed laser is used as a white light source with an average intensity of 4W from 410-2500 nm. The supercontinuum excitation light is passed through two monochromators, a

Princeton Instruments SP150 and a Princeton Instruments SP275, to provide monochromatic excitation light from the supercontinuum source. The exiting monochromatic light has a full width at half maximum bandwidth < 1 nm. Afterwards, a small part of the excitation beam is reflected to a ThorLabs S120VC calibrated silicon photodiode to continuously measure the power while the majority is focused into a 135 mm Spectralon integrating sphere (LabSphere) with a 25 mm entrance port. The liquid sample is positioned within the integrating sphere inside a polished cylindrical quartz cuvette. Light leaving the exit port of the sphere, fitted with a baffle to prevent direct reflections, is focused onto a detection monochromator and the spectrum is detected with a calibrated Princeton Instruments PIXIS 400B thermoelectrically cooled silicon CCD. The Si-CCD is wavelength calibrated by measuring the atomic lines from Hg and Ne wavelength calibration light sources, and sensitivity calibrated using a NIST-traceable radiometric calibration lamp from Ocean Optics (model HL3-plus). For relative measurements, photoluminescence quantum yields are estimated according to standard procedures using the FluoroLog.

Photoluminescence Lifetimes (TRPL)
Time resolved photoluminescence measurements (TCSPC, time-correlated single photon counting) were obtained using a PicoQuant Fluotime 300, equipped with a PMA 175 detector, PicoHarp counting card, and an LDH-P-C-405 diode laser with an excitation wavelength of 407.1 nm. The laser diode can reach repetition rates up to 80 MHz, however repetition rates were adjusted as appropriate to observe the full excited state decay.

Transmission Electron Micrographs (TEM)
TEM images were obtained using a FEI Tecnai T20 S-Twin TEM operating at 200 kV with a LaB_6 filament. Micrographs were acquired using a Gatan Orius SC200 camera. TEM samples were cast from dilute (OD < 0.2) solutions in toluene or hexanes onto Electron Microscopy CF400-Cu 400 mesh standard carbon TEM grids.

Nuclear Magnetic Resonance (NMR) Spectra
NMR spectra of micromolar concentrations of $CsPbBr_3$ NCs were measured on a 400 MHz instrument in deuterated toluene. Quantitative measurements were collected after tuning the probe and determining the 90° radio frequency pulse. Following the measurement, the concentrations were determined by comparing against an internal standard, mesitylene, at a known concentration and determining the concentration of quantum dots present in solution.

Determination of Fraction of $CsPbBr_3$ Remaining
To determine the amount of $CsPbBr_3$ remaining as the etching reaction progressed, the time-dependent steady-state absorption spectra were analyzed. There are two species to monitor, $CsPbBr_3$ and the lead-depleted phase Cs_4PbBr_6 material. For the $CsPbBr_3$ material there are two absorption regions that have no size-dependent features: 325 – 345 nm and 415 – 455 nm. To avoid contributions from Cs_4PbBr_6 we monitor the change in absorption near 425 nm and correlate the amount of $CsPbBr_3$ present using the absorption coefficient.

Additional Supporting Figures:

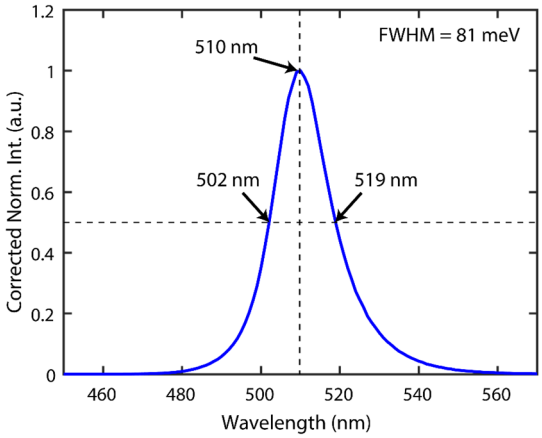

Figure S1: Photoluminescence spectra of the typical $CsPbBr_3$ nanocrystal cubes as-isolated from the reaction mixture. The linewidth of the ensemble is 17 nm (81 meV) and centered at 510 nm.

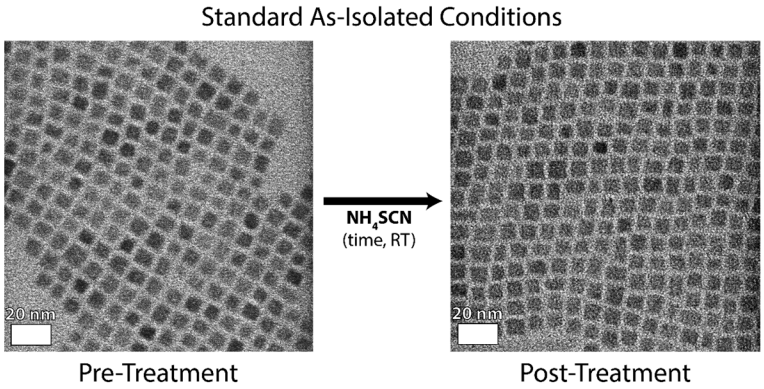

Figure S2: For as-isolated $CsPbBr_3$ nanocrystal cubes, with the as-isolated ligand concentration, there is very little, if any, change in the particle size or shape following a room temperature treatment with ammonium thiocyanate, highlighted in the TEM images of the samples.

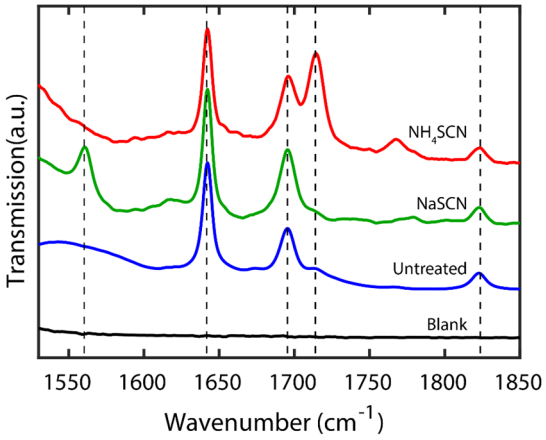

Figure S3: Infrared spectra of the liquid samples in the 1530 cm^{-1} to 1850 cm^{-1} wavenumber region. Representative samples included in the plot are the hexanes blank, untreated $CsPbBr_3$ nanocrystal cubes, sodium thiocyanate treated sample, and ammonium thiocyanate treated sample. When treating with sodium thiocyanate there is a characteristic peak that appears at 1560 cm^{-1}, and when treating with ammonium thiocyanate there is a characteristic peak that appears at 1712 cm^{-1}.

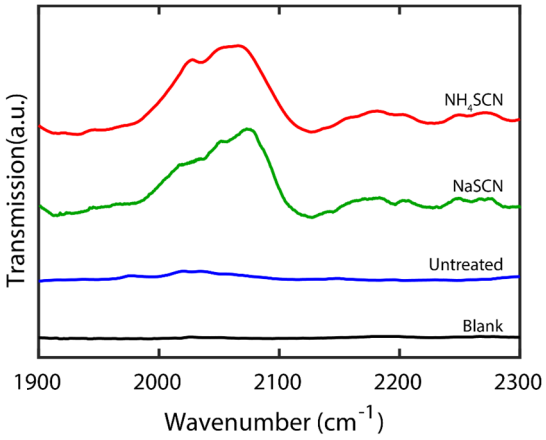

Figure S4: Infrared spectra of the liquid samples in the 1900 cm^{-1} to 2300 cm^{-1} wavenumber region. Representative samples included in the plot are the hexanes blank, untreated $CsPbBr_3$ nanocrystal cubes, sodium thiocyanate treated sample, and ammonium thiocyanate treated sample. The treatment results in characteristic vibrational peaks that appear around 2060 cm^{-1} that correspond to the cyano- stretching mode when bound to lead.

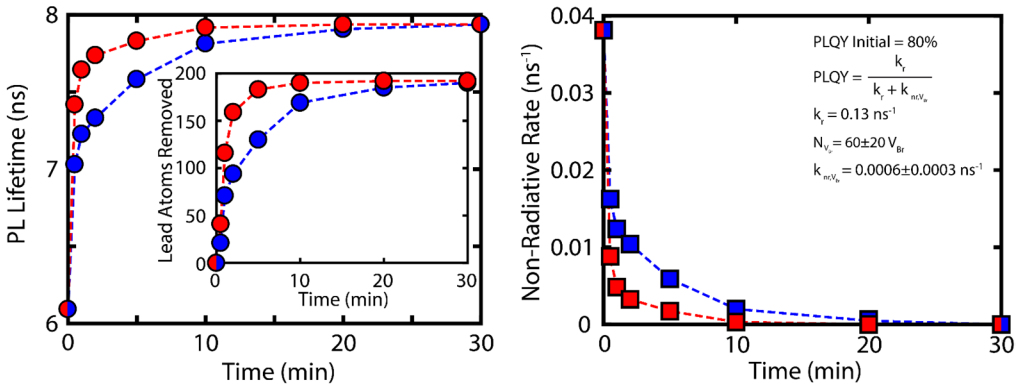

Figure S5: Determination of the non-radiative contribution per bromine vacancy, resulting in an under-coordinated lead atom that acts as a shallow electron state for a $CsPbBr_3$ sample with an initial PLQY of 80 ± 2.5%. The combination of photoluminescence excited state lifetime, the number of lead atoms removed from the average nanocrystal determined using quantitative IR, and photoluminescence quantum yield allows us to monitor the progress of the etching. This was conducted using both ammonium (red lines) and sodium thiocyanate (blue lines). We assume that the defect sites act independently of each other, i.e. they linearly contribute to the non-radiative rate ($k_{nr,Total} = N_{V_{Br}} k_{nr,V_{Br}}$). In order to capture the change in PL Lifetime with a linear contribution of each defect state, we find that more lead atoms are removed than there are under-coordinated lead atoms present. By combining these measurements, we determined the number of bromine vacancies ($N_{V_{Br}}$) and non-radiative contribution per bromine vacancy ($k_{nr,V_{Br}}$). While there are ~190 lead atoms removed during the etching reaction under as-isolated ligand conditions, this only represents ~3% of the total number of lead atoms present in the average nanocrystal, strongly suggesting that not all the ligands present in the as-isolated samples are available to participate in the etching reaction.

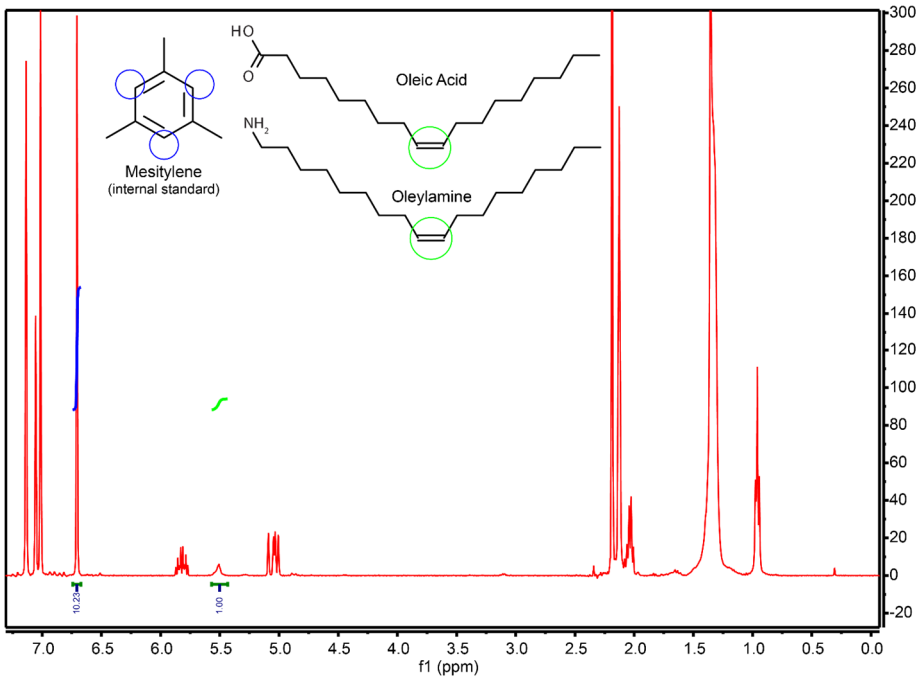

Figure S6: NMR spectra of the typical as-isolated $CsPbBr_3$ nanocrystal cubes. In order to determine the concentration of ligands (~5.5 ppm) present we compare to the mesitylene internal standard (~6.7 ppm). The alkene region contains contributions from both oleic acid and oleylamine. Here we assume that there

are equal concentrations of oleic acid and oleylamine present in the solution. For this measurement 5 µL of mesitylene was added to a 0.5 mL solution of 0.75 nanomoles of $CsPbBr_3$ nanocrystal cubes in d_6-toluene. For the measurement of typical as-isolated $CsPbBr_3$ nanocrystal cubes, we find that there is around 6 Oleic Acid and 6 Oleylamine ligands present per square nanometer of nanocrystal surface area. However, at these conditions we find that only ~190 lead atoms from a 10 nm edge length nanocrystal are removed on average. The removal of 190 lead atoms only represents ~5% of the number of ligands available in solution.

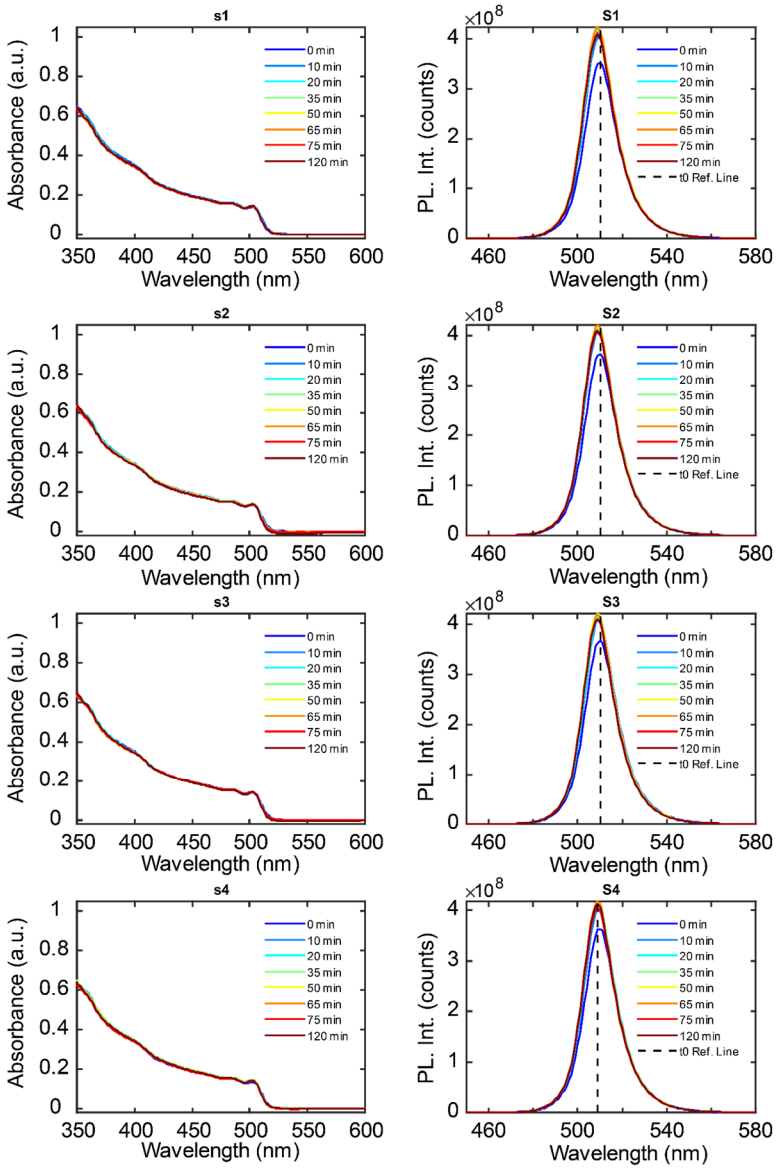

Figure S7: The absorption (left column) and corresponding photoluminescence (right column) spectra from a time series in which each set of spectra shows the as-isolated sample with increasing oleic acid concentration present in solution. Each sample had ~6 oleylamine/nm^2; then (A) had 8 oleic acid/nm^2, (B) had 10 oleic acid/nm^2, (C) had 12 oleic acid/nm^2, and (D) had 14 oleic acid/nm^2.

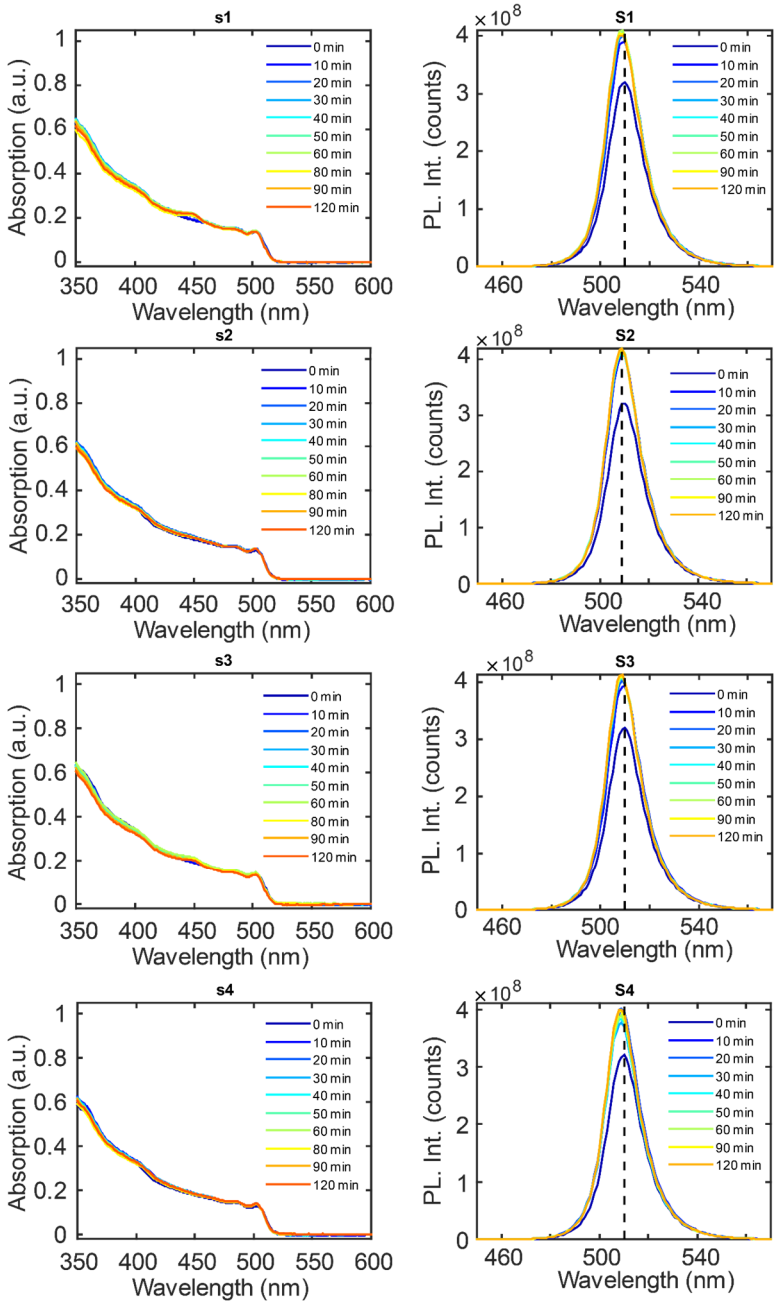

Figure S8: The absorption (left column) and corresponding photoluminescence (right column) spectra from a time series in which each set of spectra shows the as-isolated sample with increasing oleylamine concentration present in solution. Each sample had ~6 oleic acid /nm^2; then (A) had 8 oleylamine/nm^2, (B) had 10 oleylamine/nm^2, (C) had 12 oleylamine/nm^2, and (D) had 14 oleylamine/nm^2.

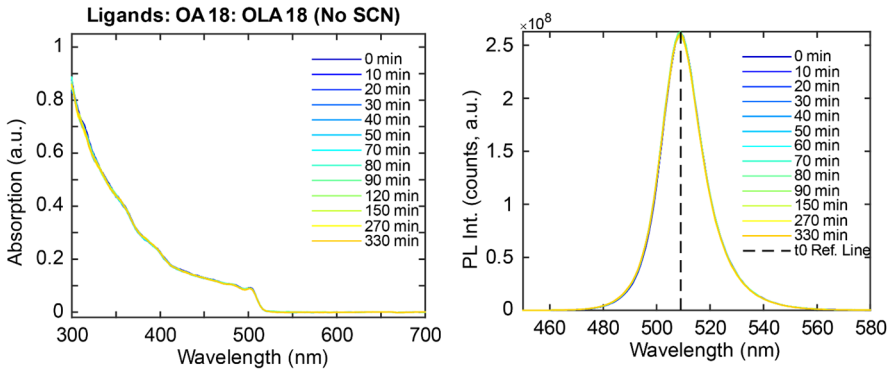

Figure S9: Control run to test the sensitivity of the $CsPbBr_3$ nanocrystals to the increased ligand concentration present in solution. Shown are the absorption (left) and the photoluminescence (right) spectra for a time series in which there were 18 oleic acid/nm² and 18 oleylamine/nm². For these samples no thiocyanate etchant was added into the sample.

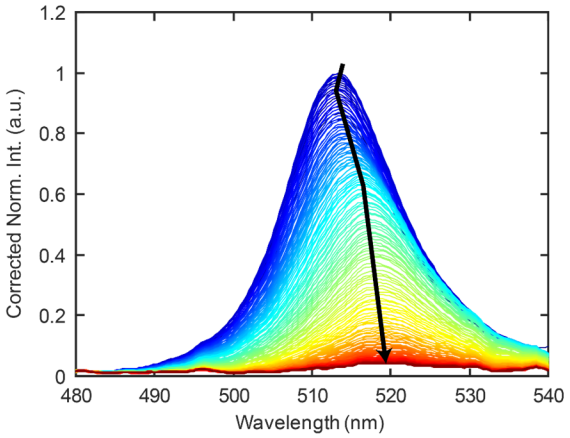

Figure S10: Depiction of the evolution of the photoluminescence spectra of a $CsPbBr_3$ nanocrystal cube sample when etched with thiocyanate. This behavior is typical of a sample that does not have enough ligands present in solution to maintain a high level of colloidal stability as the etching reaction progresses. For this sample there was initially a characteristic blue shift, however the particles began to aggregate and fall out of solution. The characteristic red-shift in the nanoparticle ensemble is indicative of this aggregation. The sample was stirred continuously to ensure no issues arose pertaining to nanoparticles settling to the bottom of the cuvette.

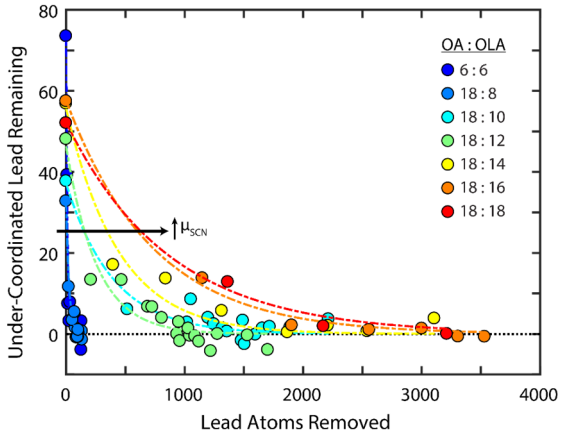

Figure S11: Depiction of the number of under-coordinated lead atoms remaining versus the total number of lead atoms removed under an increasing thiocyanate chemical potential (blue to red). By increasing the chemical potential, the selectivity in the reaction is lost, requiring more lead atoms to be removed from the particles before they remove all the under-coordinated lead atoms. This highlights the need to get the right chemical potential to increase the reaction selectivity.

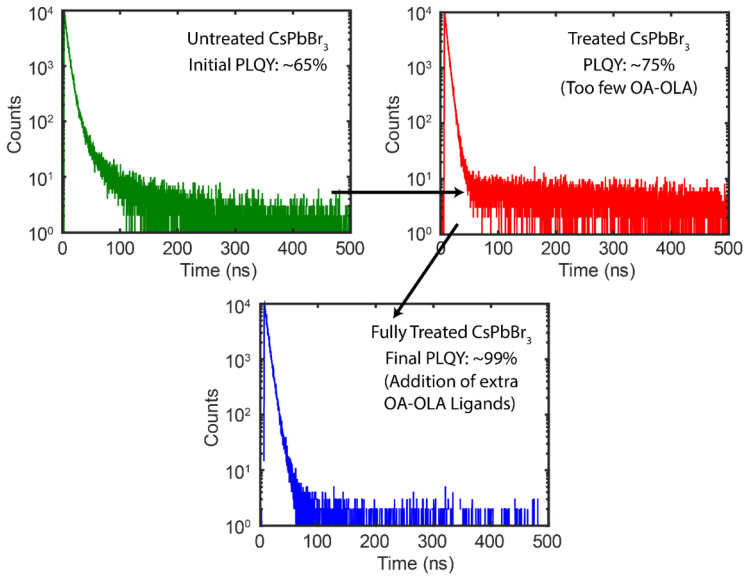

Figure S12: Depiction of the change in the photoluminescence excited state decay and quantum yield for a treatment of ~65% PLQY particles that have an insufficient number of OA-OLA ion pairs to solubilize enough thiocyanate (green to red), reaching a PLQY of ~75%. The long tail that appears as a second component in the excited state decay is also indicative of incomplete etching. By further increasing the OA-OLA ligand concentration in solution we can etch further and reach a final PLQY of near-unity (red to blue). By tailoring the concentration of OA-OLA ion pairs present in solution for the etching, we can take untreated particles and push them to fully treated particles (green to blue).

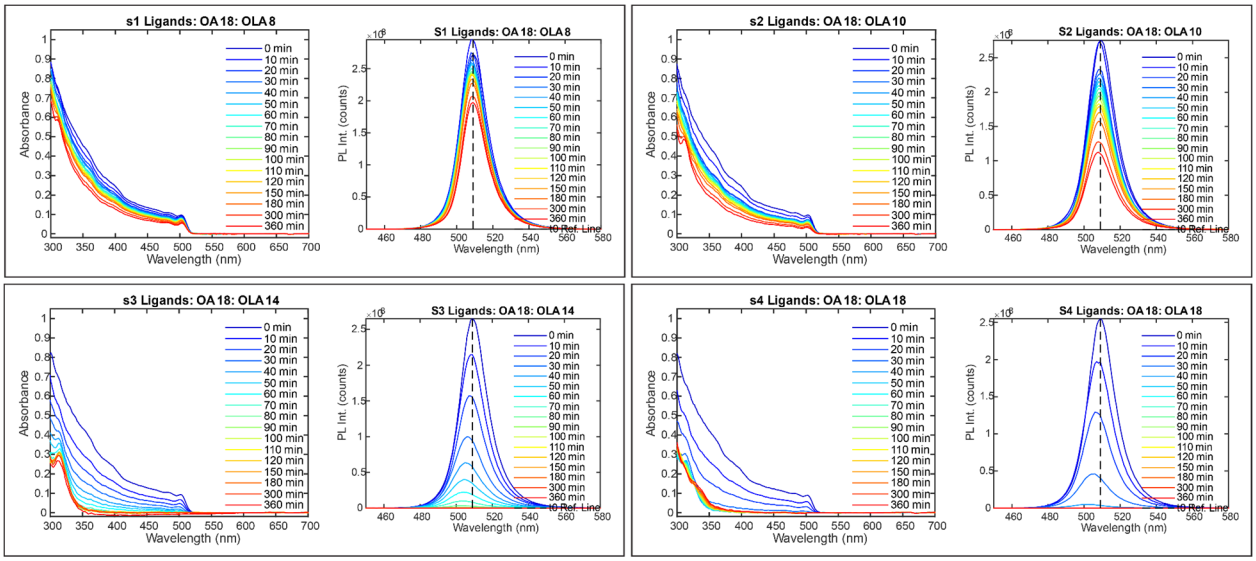

Figure S13: Change in the absorption and photoluminescence spectra for samples etched with thiocyanate containing a constant 18 oleic acid/nm² and a varying (A) 8 oleylamine/nm², (B) 10 oleylamine/nm², (C) 14 oleylamine/nm², and (D) 18 oleylamine/nm². By increasing the aggressiveness of the etching reaction, we observe a systematically larger blue shift in the photoluminescence bandgap as the etching reaction progresses, indicative of the particle size shrinking throughout the etching reaction.

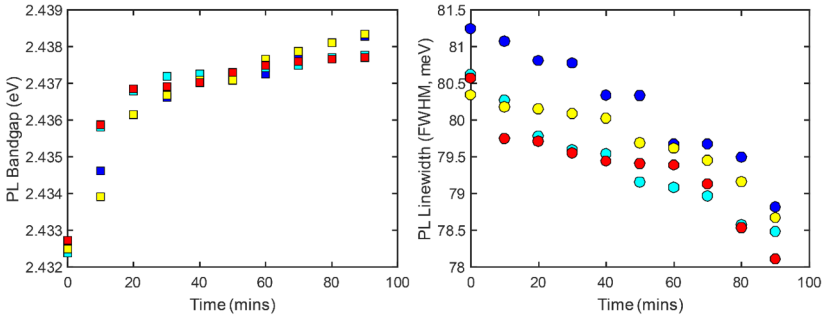

Figure S14: Depiction of the change in the photoluminescence bandgap and the photoluminescence linewidth of four samples of $CsPbBr_3$ exposed to different thiocyanate chemical potentials. In each etching reaction there is a systematic blueshift of the photoluminescence bandgap and subtle narrowing of the photoluminescence linewidth, indicative of not only a subtle etching, but also a size-dependent etching reaction in which larger particles are etched at a faster rate than smaller particles.

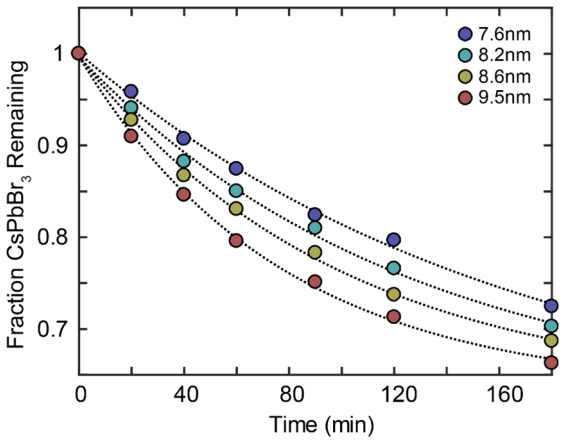

Figure S15: Size-dependent etching rate of $CsPbBr_3$ nanocrystal cubes. Shown are the trajectories of a 7.6 nm, 8.2 nm, 8.6 nm, and 9.5 nm average size ensemble exposed to 18 oleic acid/nm^2 and 12 oleylamine/nm^2.

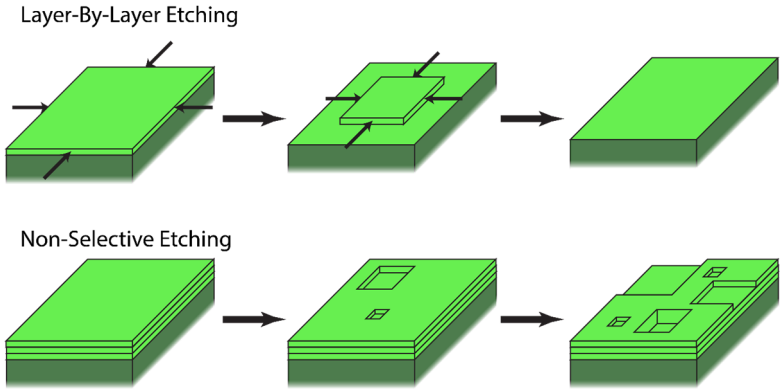

Figure S16: Depiction of the layer-by-layer etching reaction versus a non-selective random etching reaction.

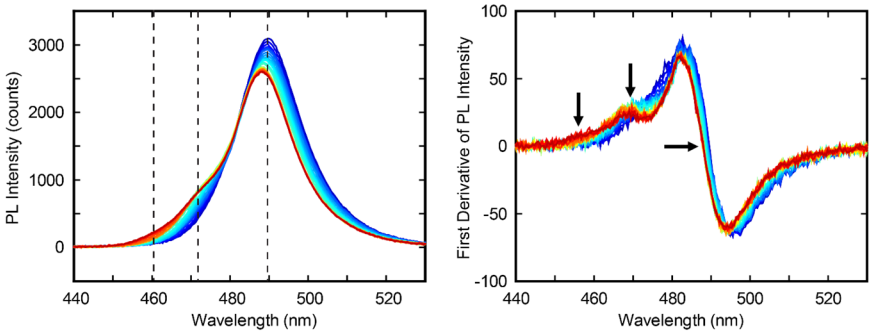

Figure S17: Change in the photoluminescence spectra of a 5-monolayer thick $CsPbBr_3$ nanoplate sample during the etching reaction showing first, the gradual increase in a peak related to the 4-monolayer thick nanoplate, and then later, the same for the 3-monolayer thick nanoplate. The emergence of these peaks can be seen in the first derivative of the photoluminescence spectra in which two clear features and a third subtle feature emerge.

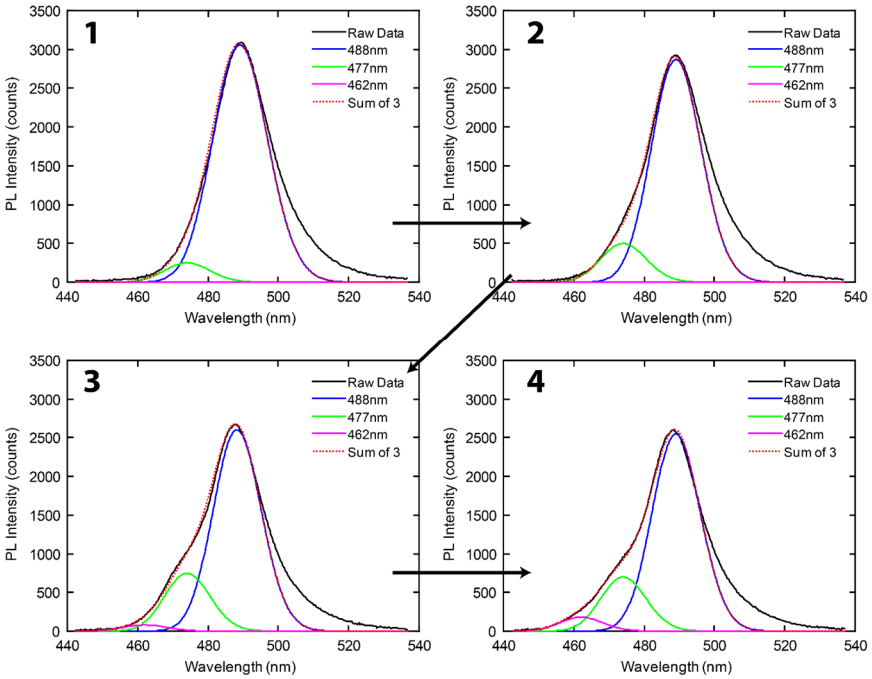

Figure S18: Identified components of the photoluminescence spectra of the ensemble of nanoplates etching in Figure S17. In the spectra there is a related peak centered at 488 nm (blue line), 477 nm (green line), and 462 nm (pink line). The intensities of these peaks are varied to reconstruct the blue-edge of the photoluminescence spectra (dotted red line).

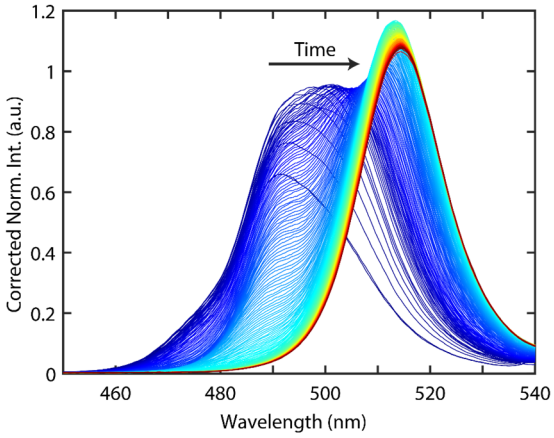

Figure S19: Change in the photoluminescence spectra of a $CsPbBr_3$ nanoplate sample when exposed to too large of an etching chemical potential. The plates quickly aggregate resulting in a substantial redshift of the photoluminescence spectra before the ensemble begins to lose photoluminescence. This highlights the need to carefully etch nanoplates to maintain isolated, well-defined nanoplates.

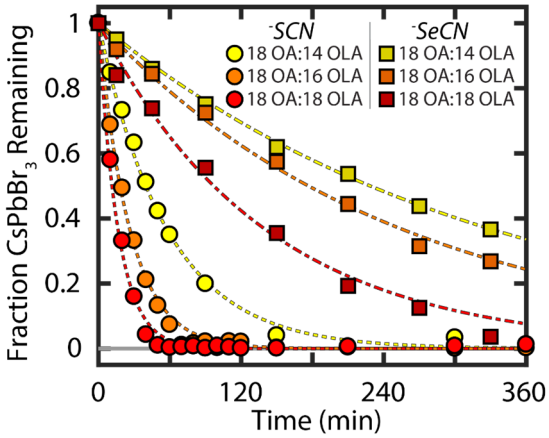

Figure S20: Change in the etching rate of thiocyanate ($^-$SCN) versus selenocyanate ($^-$SeCN) while exposed to the same OA-OLA ion pair concentrations. The selenocyanate is systematically slower than the thiocyanate at the same ligand concentration, consistent with the notion that the chemical potential of the etchant is crucial in dictating the extent of etching and is modulated by the hardness or softness of the chemical etchant.